Nano Research 2018, 11(9): 4796–4805
https://doi.org/10.1007/s12274-018-2065-1
Research Article

ISSN 1998-0124
CN 11-5974/O4

Molten-salt synthesis of porous $La_{0.6}Sr_{0.4}Co_{0.2}Fe_{0.8}O_{2.9}$ perovskite as an efficient electrocatalyst for oxygen evolution

Sanzhao Song[1,2,§], Jing Zhou[1,§], Shuo Zhang[1] (✉), Linjuan Zhang[1], Jiong Li[1], Yu Wang[1], Ling Han[1], Youwen Long[3,4], Zhiwei Hu[5], and Jian-Qiang Wang[1,2] (✉)

[1] *Shanghai Institute of Applied Physics, Chinese Academy of Sciences, Shanghai 201800, China*
[2] *University of Chinese Academy of Sciences, Beijing 100049, China*
[3] *Beijing National Laboratory for Condensed Matter Physics, Institute of Physics, Chinese Academy of Sciences, Beijing 100190, China*
[4] *Collaborative Innovation Center of Quantum Matter, Beijing 100190, China*
[5] *Max Planck Institute for Chemical Physics of Solids, Nöthnitzer Strasse 40, Dresden 01187, Germany*
[§] *Sanzhao Song and Jing Zhou contributed equally to this work.*

Received: 18 January 2018
Revised: 7 March 2018
Accepted: 24 March 2018

KEYWORDS

iron-rich,
perovskite,
oxygen evolution reaction,
energy storage and conversion,
molten salt

ABSTRACT

The development of an efficient and low-cost electrocatalyst for the oxygen evolution reaction (OER) via an eco-efficient route is a desirable, although challenging, outcome for overall water splitting. Herein, an iron-rich $La_{0.6}Sr_{0.4}Co_{0.2}Fe_{0.8}O_{2.9}$ (LSCF28) perovskite with an open porous topographic structure was developed as an electrocatalyst by a straightforward molten-salt synthesis approach. It was found that porosity correlates with both the iron content and the molten-salt approach. Benefiting from the large surface area, high activity of the porous internal surface, and the optimal electronic configuration of redox sites, this inexpensive material exhibits high performance with a large mass activity of 40.8 $A\cdot g^{-1}$ at a low overpotential of 0.345 V in 0.1 M KOH, surpassing the state-of-the-art precious metal IrO_2 catalyst and other well-known perovskites, such as $Ba_{0.5}Sr_{0.5}Co_{0.8}Fe_{0.2}O_3$ and $SrCoO_{2.7}$. Our work illustrates that the molten-salt method is an effective route to generate porous structures in perovskite oxides, which is important for energy conversion and storage devices.

1 Introduction

The insufficiency of fossil fuels and the increasing concern over pollution problems associated with their use have encouraged significant research efforts towards the exploration of advanced energy systems with low-cost, abundant, and environmentally friendly materials [1–3]. Electrochemical water splitting is regarded as a promising approach for energy storage and conversion; it utilizes electric energy to split

---

Address correspondence to Shuo Zhang, zhangshuo@sinap.ac.cn; Jian-Qiang Wang, wangjianqiang@sinap.ac.cn

abundant water into clean H_2 fuel [4, 5]. The oxygen evolution reaction (OER), which involves a complex four-electron transfer, plays a central role in this electrochemical process. The kinetics of OER are sluggish and often require a considerably high overpotential relative to the thermodynamic potential of the reaction (1.23 V vs. a reversible hydrogen electrode (RHE) at standard temperature and pressure) to reach a desirable current density, such as 10 $mA\cdot cm^{-2}$ (on the basis of 10% solar-to-fuel conversion efficiency) [6]. Therefore, the development of catalysts to overcome the high energy barrier of O–O bond formation in commercial devices is constantly being pursued [7, 8]. Among the materials tested thus far, ruthenium and iridium oxides exhibit the best overall performance; however, their use is limited by their scarcity and high cost. Thus, it is mandatory to develop alternative OER electrocatalysts that are inexpensive, sufficiently active, and stable upon prolonged exposure to oxidizing conditions in alkaline solutions [9–11].

Among the wide variety of metal oxides available, the crystal family of perovskite oxides $ABO_{3+\delta}$, in which A is a rare-earth or alkaline-earth element and B is a transition metal, are attractive candidates due to their high ionicity, electronic conductivity, and structural stability [12, 13]. Moreover, both A and B sites can be readily doped with electrons and holes using elements of varying valency, electronegativity, or ionic size to tune the structural, physical, and electronic properties of the catalyst [14–17]. Recently, Suntivich et al. proposed a descriptor for the rational design of perovskite electrocatalysts with high OER activity; in other words, a near-unity occupancy of the e_g orbital of the first-row transition metal in perovskite oxides can enhance the intrinsic activity of the OER in alkaline solutions [18–20]. After their proposal, Co-based perovskite oxides attracted particular interest owing to the spin degree of freedom of Co^{3+} and Co^{4+} ions with different e_g occupancies. Indeed, excellent intrinsic OER activities were observed for $LiCo_{0.8}Fe_{0.2}O_3$, $LaCoO_3$, $Ba_{0.5}Sr_{0.5}Co_{0.8}Fe_{0.2}O_{3-\delta}$ (BSCF), $SrCoO_{2.7}$, and $SrNb_{0.1}Co_{0.7}Fe_{0.2}O_{3-\delta}$ among others [16, 21–25]. Double-perovskite $(Ln_{0.5}Ba_{0.5})CoO_{3-\delta}$ (Ln = Pr, Sm, Gd, and Ho) and quadruple-perovskite $CaCu_3Fe_4O_{12}$ were also found to be highly active catalysts [26, 27]. However, several disadvantages limit their practical applications, including poor mass activity (MA), heavy use of expensive and toxic elemental cobalt, and energy-intensive synthesis. The typical synthesis conditions for perovskites usually require high temperatures (> 800 °C) and long (> 10 h) sintering periods [28]. This process leads to materials with a typical size of several micrometers and thus, poor MA. These characteristics are far from those desired for practical applications. Even though further treatment techniques, such as ball milling, can largely improve the activity of the produced perovskite [25], the complicated process, increased energy consumption, and low productivity limit its application. Therefore, there is an urgent need to develop highly OER-active perovskite oxides using earth-abundant and environmentally friendly elements to partially replace the expensive and toxic elemental cobalt and to realize mass production through an economical alternate route.

In this work, taking full advantage of the feature of fast ion diffusion in molten salts, we synthesized an iron-rich perovskite, $La_{0.6}Sr_{0.4}Co_{0.2}Fe_{0.8}O_{2.9}$, with an open and porous topographic structure; further, it possesses a large specific surface area of 26 $m^2\cdot g^{-1}$. This low-cost material can effectively catalyze water oxidation with a large MA of 40.8 $A\cdot g^{-1}$ at a small overpotential (η) of 0.345 V, which is 1.7 times higher than that of the state-of-the-art IrO_2 electrocatalyst. The porous internal surface has a much higher OER activity than the external surfaces of the particles, owing to which it contributes more to such high OER performance. It was found that the cooperative effect of both cobalt and iron ions leads to a better OER performance, i.e., the optimal electronic structure of cobalt and the porous structure induced by iron ions provides an abundance of redox sites. More importantly, the molten-salt approach is economically advantageous for the mass production of highly OER-active perovskite oxides.

2 Experimental

2.1 Synthesis of $La_{0.6}Sr_{0.4}Co_{1-x}Fe_xO_{3-\delta}$

$La_{0.6}Sr_{0.4}Co_{1-x}Fe_xO_{3-\delta}$ (x = 0, 0.2, 0.5, 0.8, and 1) was synthesized using the molten-salt method. The metal precursors La_2O_3 (99.9%, Alfa Aesar), $SrCO_3$ (99.9%, Alfa Aesar), Co_3O_4 (99.9%, Alfa Aesar), and Fe_3O_4 (99.9%, Alfa Aesar) were used as received without any further purification. Alkali metal chlorides, NaCl (Aladdin, 99.9%) and KCl (Aladdin, 99.9%), were dried at 100 °C for 24 h. Subsequently, an eutectic mixture, with a melting point of 657 °C, was produced by mixing dried NaCl and KCl in an agate mortar at a molar ratio of 1:1. The quantities of the metal precursors were calculated to obtain 0.025 mol of $La_{0.6}Sr_{0.4}Co_{1-x}Fe_xO_{3-\delta}$ (x = 0, 0.2, 0.5, 0.8, and 1, denoted as LSC, LSCF28, LSCF55, LSCF82, and LSF, respectively). The weight ratio of the mixed oxide and molten salt was maintained at 1:2. Perovskite synthesis was carried out in alumina crucibles placed in a tube furnace and heated using a temperature-programmable furnace. In order to complete the reaction, the molten mixtures were heated at 850 °C for 5 h. After cooling, the soluble compounds of the reaction mixtures were dissolved in distilled water and the solid product was centrifuged and washed repeatedly. Finally, the samples were dried in vacuum overnight at 60 °C to remove the remaining water.

$La_{0.6}Sr_{0.4}Co_{0.2}Fe_{0.8}O_{3-\delta}$ was also synthesized according to a traditional solid-state reaction route (denoted as LSCF28-SS). Briefly, the metal precursors La_2O_3 (99.9%, Alfa Aesar), $SrCO_3$ (99.9%, Alfa Aesar), Co_3O_4 (99.9%, Alfa Aesar), and Fe_3O_4 (99.9%, Alfa Aesar) were weighed, mixed, and milled in a planetary mill using ethanol as the solvent at 400 rpm for 1 h. After drying, the powder mixtures were calcined at 1,200 °C in air for 5 and 10 h to form perovskite oxides.

2.2 Physicochemical characterization

The composition of the synthesized perovskite materials was determined by inductively coupled plasma optical emission spectrometry (ICP-OES) with a Spectro ARCOS ICP-OES (Spectro Analytical Instruments, Kleve, Germany) instrument with axial plasma viewing. X-ray diffraction (XRD) patterns were recorded using a Bruker D8 Advance X-ray diffractometer (Bruker, Germany) with nickel-filtered Cu Kα (λ = 1.54178 Å) radiation in the scanning angle (2θ) range of 20°–80° at a scanning speed of 2 $°\cdot min^{-1}$ and operating voltage and current of 40 kV and 40 mA, respectively. Scanning electron microscopy (SEM) was conducted using a ZEISS Merlin Compact Field Emission Scanning Electron Microscope with an acceleration voltage of 5 kV. The specific surface areas of the catalysts were evaluated using a Brunauer–Emmet–Teller (BET) analysis system with an N_2 adsorption medium.

2.3 Synchrotron radiation X-ray spectroscopy measurements

The Co and Fe K-edge extended X-ray absorption fine structure (EXAFS) data were analyzed at the 14W beam line of the Shanghai Synchrotron Radiation Facility (SSRF). The measurements were carried out with a Si (111) double-crystal monochromator in the transmission mode. The Co and Fe $L_{2,3}$-edge X-ray absorption spectra (XAS) were collected at room temperature at the 11A beamline of the "National Synchrotron Radiation Research Center (NSRRC)" in Taiwan, China, with photon energy resolutions of about 0.3 and 0.25 eV, respectively. Pellet samples were fractured *in situ* in an ultrahigh-vacuum chamber at pressures in the range of 10^{-10} mbar.

2.4 Electrochemical measurements of the OER activities

Electrochemical measurements were performed at room temperature using a rotating disk working electrode (RDE) made of glassy carbon (PINE, 5 mm diameter, 0.196 cm^2) and connected to a PGSTAT 302N (Metrohm Autolab) electrochemical system. The glassy carbon (GC) electrode was pre-polished with α-Al_2O_3 slurries of different diameters in a sequential manner (1.0 μm, 0.3 μm, and 50 nm) on a polishing cloth and sonicated in ethanol for 5 min. The electrodes were finally rinsed with deionized water and dried before each test. A Pt wire placed in a fritted glass tube and Ag/AgCl (3.5 M KCl) were used as the counter and reference electrodes, respectively. All the potentials measured were calibrated to the RHE potential using the following equation: $E_{RHE} = E_{Ag/AgCl} + 0.197\ V + 0.059pH$. The working electrodes containing the investigated catalysts were prepared as follows. Electrocatalyst powder (5 mg) was dispersed in 1 mL of a 3:1 (v/v) deionized (DI)-water/isopropanol mixed solvent with 40 μL Nafion (5 wt.%, Sigma-Aldrich); later, this mixture was sonicated in an ultrasonic water bath for about 1 h. Subsequently, 10 μL of the dispersion was dropped onto a glassy carbon disk (5 mm diameter), leading to a catalyst loading of about 0.245 mg·cm^{-2}. Finally, the as-prepared electrode was dried at room temperature. For long-term stability tests, carbon paper was used as the working electrode and the catalyst loading was maintained constant.

The electrolyte consisted of 0.1 M KOH aqueous solution (99.99% metal purity, pH ~ 12.7), which was saturated with O_2 for 30 min prior to each test and maintained under O_2 atmosphere throughout. Linear sweeping voltammograms (LSVs) were constructed using a RDE at 1,600 rpm in O_2-saturated 0.1 M KOH at a scan rate of 5 mV·s^{-1} from 0 to 0.9 V vs. Ag/AgCl (3.5 M KCl). All the potential values were iR-corrected to compensate for the effect of solution resistance using the following equation: $E_{\text{iR-corrected}} = E - iR$, where i is the current and R is the uncompensated ohmic electrolyte resistance (~ 45 Ω) measured via high-frequency alternating current (AC) impedance in O_2-saturated 0.1 M KOH. Accelerated stability tests were performed in O_2-saturated 0.1 M KOH by potential cycling between 0 and 0.6 V vs. Ag/AgCl at a scan rate of 10 mV·s^{-1} for 1,000 cycles.

3 Results and discussion

The ICP-OES results of $La_{0.6}Sr_{0.4}Co_{1-x}Fe_xO_{3-\delta}$ (LSCF) synthesized by the molten-salt method are summarized in Table S1 in the Electronic Supplementary Material (ESM). The La:Sr and Fe:Co ratios in all the samples are close to their raw ratio. Figure 1(a) shows the XRD patterns of molten-salt-synthesized $La_{0.6}Sr_{0.4}Co_{1-x}Fe_xO_{3-\delta}$. It was found that the perovskite-type structure is always the main phase, which can be indexed with the space group $R3c$ [29–31]. The XRD pattern of $La_{0.6}Sr_{0.4}CoO_{3-\delta}$ (LSC) exhibits two peaks in the region between 32° and 35°, corresponding to the *hkl* planes of (110) and (104), respectively, as shown in JCPDS No. 36-1393 [32]. There is only a single peak in the LSF sample, akin to the peak information in JCPDS No. 82-196 [33]. In addition, we clearly observed that with an increase in the iron content, a notable shift of the diffraction line toward lower 2θ angles occurred, as shown in the right-hand panel of Fig. 1(a). The shift in the diffraction peaks correlates with the iron content and demonstrates that the unit cell parameters increase with interchanging cobalt and iron ions [34].

To further shed some light on this issue, we conducted EXAFS measurements at the Fe and Co K

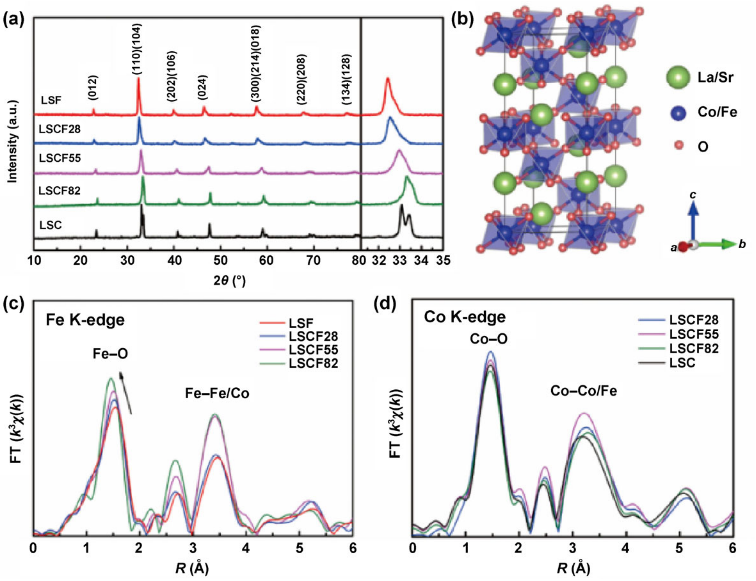

Figure 1 (a) XRD patterns of the $La_{0.6}Sr_{0.4}Co_{1-x}Fe_xO_{3-\delta}$ (LSCF) powder; an expanded view of the 31°–35° 2θ region is shown on the right. (b) LSCF crystal structure (La and Sr have the same positions, which are denoted by green, while Co and Fe are denoted by blue and O by red). (c) Fourier transforms of the experimental EXAFS spectra of LSF, LSCF28, LSCF55, and LSCF82. (d) Fourier transforms of the experimental EXAFS spectra of LSCF28, LSCF55, LSCF82, and LSC. None of the Fourier transforms are corrected for phase shift.

edges, as shown in Figs. 1(c) and 1(d), respectively. It can be observed that with increasing Fe content, the Fe–O bond length gradually increased, while the Co–O bond length remained almost constant (Table S2 in the ESM). From these observations, we concluded that the variation in unit cell parameters can be attributed to the changes in the Fe–O distance. Furthermore, it may also be ascribed to the larger ionic radius of Fe(III) ions (0.645 Å) compared to Co(III) ions (0.61 Å) [35]. More importantly, it was found that the molten-salt method allows us to achieve the desired $La_{0.6}Sr_{0.4}Co_{1-x}Fe_xO_3$ crystalline phase at significantly lower temperatures (850 °C) and in shorter time periods (5 h). In contrast, the conventional solid-state route for synthesizing $La_{0.6}Sr_{0.4}Co_{0.2}Fe_{0.8}O_{3-\delta}$ (LSCF28-SS) requires a high temperature of 1,200 °C and long experimental run of 10 h to achieve a well-formed crystalline phase (Fig. S1 in the ESM).

The electrocatalytic activities of the synthesized perovskites and IrO_2 for the OER were evaluated by constructing LSVs in O_2-saturated 0.1 M KOH at a scan rate of 5 $mV\cdot s^{-1}$ and rotation speed of 1,600 rpm, as shown in Fig. 2(a). The potential is referenced to a RHE, which was calibrated as described in the Experimental section. All the potential values were *iR*-corrected for each LSV to compensate for the resistance of the solution. The key parameters are summarized in Table 1. It is clear that LSCF28 exhibits the best OER activity; for instance, it exhibits a small onset potential of 1.50 V, which is much lower than those of other samples. Moreover, the corresponding Tafel plots displayed in Fig. 2(b) also indicate that LSCF28 exhibits the smallest Tafel slope of 70 $mV\cdot dec^{-1}$. This allows LSCF28 to achieve a current density of 10 $mA\cdot cm^{-2}$ at a comparably small η value of 0.345 V, which is not only lesser than those of LSCF55 (η = 0.373 V), LSCF82 (η = 0.39 V), LSF (η = 0.422 V), and LSC (η = 0.397 V), but also lesser than that of IrO_2 (η = 0.36 V) [6, 33]. Accordingly, LSCF28 exhibits a large MA of 40.8 $A\cdot g^{-1}$ at 0.345 V, which is 1.7 times higher than that of IrO_2, as depicted in Fig. 2(c). In addition, the LSCF28 electrocatalyst shows higher activity than several other recently reported high-performance OER catalysts, such as $Ba_{0.5}Sr_{0.5}Co_{0.8}Fe_{0.2}O_3$ [18], $SrCoO_{2.7}$ [21], $SrNb_{0.1}Co_{0.7}Fe_{0.2}O_{3-\delta}$ [25], and double-perovskite $PrBaCo_2O_{5-\delta}$ [26] (see Table S3 in the ESM). The results of the long-term stability analysis plotted in Fig. S3(a) in the ESM indicate that LSCF28 exhibits nearly identical cyclic voltammetry (CV) curves for 1,000 cycles. Moreover, we also conducted chronopotentiometry

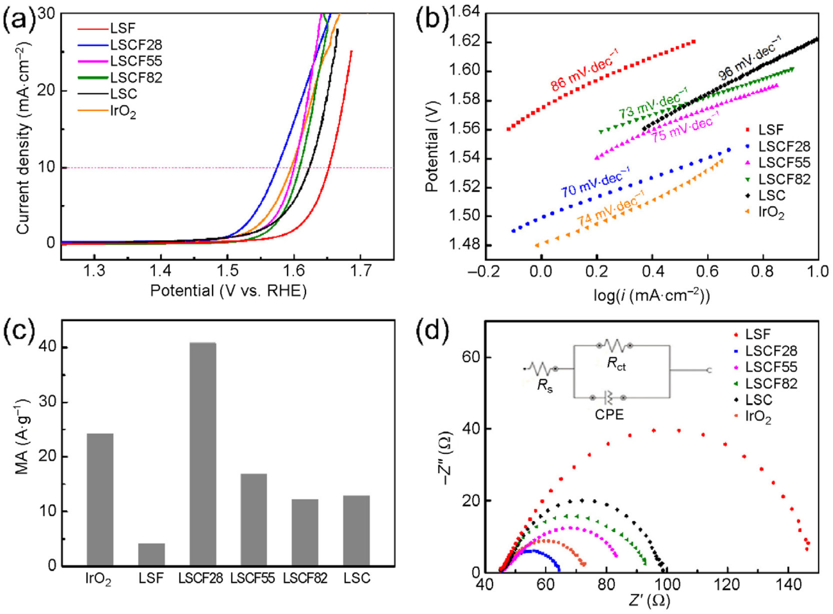

Figure 2 (a) LSVs for the OER on rotating disk electrodes consisting of $La_{0.6}Sr_{0.4}Co_{1-x}Fe_xO_{3-\delta}$ and IrO_2 catalysts in an O_2-saturated 0.1 M KOH solution at 1,600 rpm. (b) Tafel plots of the $La_{0.6}Sr_{0.4}Co_{1-x}Fe_xO_{3-\delta}$ and IrO_2 catalysts. (c) MA based on the oxide weight of the $La_{0.6}Sr_{0.4}Co_{1-x}Fe_xO_{3-\delta}$ and IrO_2 catalysts at η = 0.345 V. (d) Electrochemical impedance spectra of the $La_{0.6}Sr_{0.4}Co_{1-x}Fe_xO_{3-\delta}$ and IrO_2 electrodes recorded at 1.575 V vs. RHE at an AC voltage of 10 mV. The equivalent circuit is shown in the inset.

Table 1 Comparison of the OER activities of the synthesized perovskites in an alkaline medium

Catalyst	Onset potential (V vs. RHE)	η at 10 $mA\cdot cm^{-2}$ (V)	Tafel slope ($mV\cdot dec^{-1}$)	MA at η = 0.345 V ($A\cdot g^{-1}$)
LSC	1.55	0.399	96	12.0
LSCF82	1.52	0.390	84	13.5
LSCF55	1.52	0.373	75	19.8
LSCF28	1.50	0.345	70	40.8
LSF	1.58	0.422	86	5.0
IrO_2	1.51	0.360	74	24.7

to evaluate the catalytic durability of LSCF28 and found a nearly constant potential for over 90 h, as shown in Fig. S3(b) in the ESM. The large MA and relatively good durability of LSCF28 illustrate its potential as an efficient and low-cost OER electrocatalyst.

To gain more information on the kinetics of the OER, charge-transfer resistances were evaluated by electrochemical impedance spectroscopy (EIS) measurements; the results are shown in Fig. 2(d). Generally, the ion- and charge-transport are crucial factors in determining the performance of electrochemical OER catalysts. The synthesized perovskites exhibited good ionic and charge-transfer abilities between the electrolyte and activity material. The charge-transfer resistances (R_{ct}) were found to be 24.3, 32.5, 43.2, 52.9, 58.7, and 106.1 Ω for LSCF28, IrO_2, LSCF55, LSCF82, LSC, and LSF, respectively. LSCF28 exhibits the lowest charge-transfer resistance and hence, the fastest charge transfer of all the perovskites synthesized in the current study.

The microstructures of $La_{0.6}Sr_{0.4}Co_{1-x}Fe_xO_{3-\delta}$ samples were characterized by SEM analysis (Figs. 3(a)–3(e)). Obviously, iron content has a profound effect on the size and morphology of perovskite oxides. Compared to LSC, which has a particle size of ~ 500 nm, iron-containing samples have smaller particle sizes in the range of ~ 300 nm. LSC and LSCF82 exhibit dense structures, while LSCF55 contains a few particles with porous structures. As shown in the magnified image, the diameter of the macroporous cores is ~ 200 nm. We could observe that the number of these porous structures increases with an increase in the iron content, i.e., more LSF particles exhibit this microstructure. Considering that LSCF28-SS exhibits a dense structure with a large particle size of 1 μm (Fig. S4 in the ESM), we concluded that both the iron content and the molten-salt approach are essential for producing a porous structure in LSCF perovskite oxides.

From a structural point of view, a porous structure should have a much larger total surface area (quantified by the BET surface algorithm) than a dense structure and therefore should have a relatively larger number of active sites; however, it must be mentioned that the BET surface area is not equal to the real activearea [36, 37]. The BET surface areas of different electrolytes were measured by gas desorption (Fig. S5 in the ESM) and plotted in Fig. 3(f). As expected, LSC has the smallest surface area of about 12 $m^2\cdot g^{-1}$ among all the samples synthesized via the molten-salt approach. With increasing iron content, the BET surface areas quickly increase. Finally, LSCF28 and LSF possess large BET areas of ~ 26 and ~ 27 $m^2\cdot g^{-1}$, respectively. In general, perovskite catalysts synthesized via conventional solid-state methods typically exhibit low surface areas (< 10 $m^2\cdot g^{-1}$) owing to their high calcination temperatures (> 800 °C) [14].

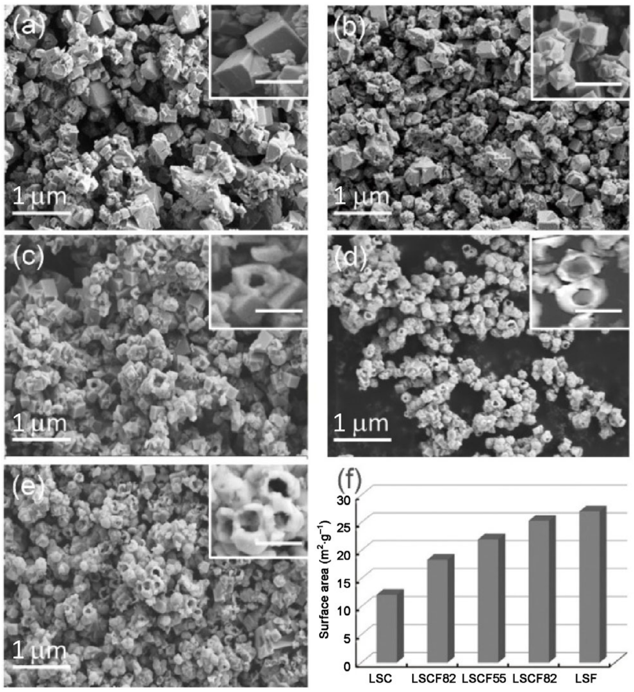

Figure 3 SEM images of $La_{0.6}Sr_{0.4}Co_{1-x}Fe_xO_{3-\delta}$. (a) LSC, (b) LSCF82, (c) LSCF55, (d) LSCF28, and (e) LSF; the insets show the corresponding magnified images at a scale of 500 nm. (f) Surface areas of the $La_{0.6}Sr_{0.4}Co_{1-x}Fe_xO_{3-\delta}$ systems.

Molten-salt synthesis, on the other hand, allows faster mass-transfer transport in the liquid phase by means of convection and diffusion, and as a result, the calcination temperature is dramatically lowered and the sintering time is shortened [38, 39]. Therefore, molten salt synthesis is advantageous in synthesizing small particles with large surface areas.

Combining the results of electrochemical and morphological investigations, we could find that the mass catalytic activity towards OER roughly correlated with the porous morphology induced by the iron content. It was found that the growing trend of mass catalytic activity is in line with the changes in the BET values. Although the BET surface areas corresponding to the gas adsorption sites are not necessarily equal to the actual active areas (as some surfaces of the active sites are not exposed), this result could still be ascribed to the increase in the total number of active sites. Nevertheless, it is to be noted that although LSF has the largest surface area, it exhibits the lowest activity. In the systems developed in this study, due to the differences in oxygen stoichiometry, structural or physic-chemical of the compared catalyst materials, we cannot definitively claim that cobalt ions serve as redox sites. Based on past reports on perovskites, such as $Ba_{0.5}Sr_{0.5}Co_{0.8}Fe_{0.2}O_{3-\delta}$ [18] and $SrNb_{0.1}Co_{0.7}Fe_{0.2}O_{3-\delta}$ [25], we speculate that the cobalt ions in our materials possibly have a similar effect.

In order to explore the effect of porous structures on the active surfaces and, in turn, the OER activities, the specific activities (SAs) (mA·cm^{-2}) of the as-prepared samples at $\eta = 0.345$ V were calculated by normalizing with the real oxide surface areas, by BET measurements. The results are plotted in Fig. 4(a). According to SEM analysis, LSCF55, LSCF28, and LSF exhibit similar porous morphologies, including the interior surfaces of porous structures and the external surfaces of particles. More importantly, an increase in the iron content dramatically increases the number of pores. Furthermore, it could be observed that the increased OER activity of LSCF correlated with an increase in its porosity. For instance, the SA of LSCF28 is 2 times more than that of LSCF82. This result does not meet the expectation that all the LSCF samples have similar SAs in spite of having similar surface areas. Hence, the additional increase in OER activity implies that there is an underlying factor. Generally, the OER activity of electrocatalysts is determined using the intrinsic activity of a single redox site and the number of redox sites. The former is strongly correlated with the electronic configuration of the redox ions at the surface, involving the valence state, spin state, and covalency. The latter is associated with the particle size and surfaces with exposed redox sites. Although we could not distinguish which factor governs the enhancement in the OER activity, we could find that the SA increased with an increase in the number of pores, illustrating the fact that the interior surface of

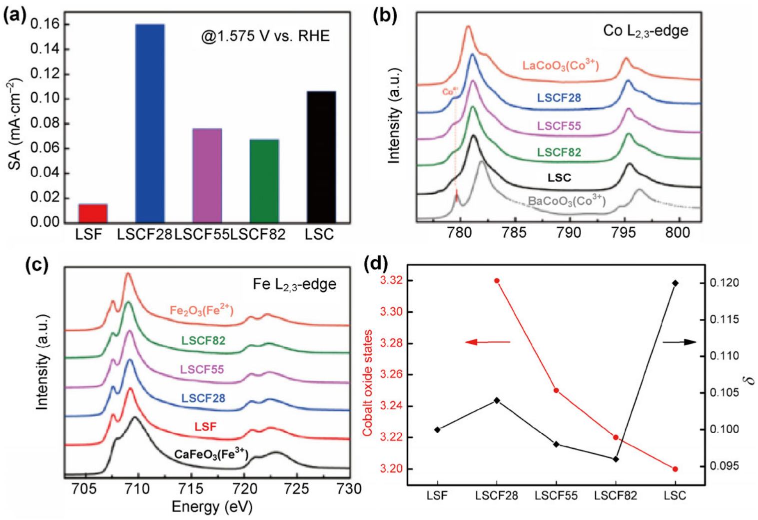

Figure 4 (a) SA of $La_{0.6}Sr_{0.4}Co_{1-x}Fe_xO_{3-\delta}$. (b) Co $L_{2,3}$-edge X-ray-absorption spectra. (c) Fe $L_{2,3}$-edge X-ray-absorption spectra. (d) The red line denotes cobalt oxide states and black line denotes oxygen vacancies in $La_{0.6}Sr_{0.4}Co_{1-x}Fe_xO_{3-\delta}$.

a porous structure benefits OER activity.

The electronic configurations of cobalt as well as iron ions were investigated by Co and Fe $L_{2,3}$-edge XAS of $La_{0.6}Sr_{0.4}Co_{1-x}Fe_xO_{3-\delta}$ together with $LaCoO_3$ and $BaCoO_3$ as Co^{3+} and Co^{4+}, respectively, and Fe_2O_3 and $CaFeO_3$ as Fe^{3+} and Fe^{4+}, respectively [40–42]. The results are shown in Figs. 4(b) and 4(c), respectively. The line shape of the XAS spectrum at the transition-metal (TM) $L_{2,3}$ edge strongly depends on the multiplet effects from the TM 3d–3d, 2p–3d Coulomb interactions, exchange interactions, and local crystal field interactions as well as hybridization with O 2p ligands [43, 44]. This makes the technique extremely sensitive to the spin, orbital, and valence states of the ions [45–49]. It was found that both Fe and Co ions possess a mixed-valence state of +3 and +4 states, which can be attributed to the charge compensation of Sr^{2+} ions. It can also be seen that the valence state of Co ions increases with increasing iron content. The average valence state was obtained by simulating the XAS spectra with reference samples (Figs. S6 and S7 and Table S4 in the ESM). The valence state of cobalt ions in LSCF28 was found to be +3.35, which is close to the optimal value of +3.4 in $SrCoO_{2.7}$, which has been reported to exhibit a high room-temperature SA and MA towards alkaline water electrolysis. Furthermore, we estimated the concentration of oxygen vacancies (represented by δ) based on the ICP results and valence states of the TMs. It is important to note that LSCF28, which can be written as $La_{0.6}Sr_{0.4}Co_{0.2}Fe_{0.8}O_{2.9}$, has a large number of oxygen vacancies, which can possibly provide an abundance of exposed redox sites [10, 50].

4 Conclusions

In summary, we report for the first time an iron-rich $La_{0.6}Sr_{0.4}Co_{0.2}Fe_{0.8}O_{2.9}$ (LSCF28) perovskite as an efficient electrocatalyst for water oxidation. These perovskites were synthesized via an eco-efficient molten-salt approach. This catalyst realizes high performance for water oxidation with a large MA of 40.8 $A\cdot g^{-1}$, low overpotential of 0.345 V, and small Tafel slope of 70 $mV\cdot dec^{-1}$ in 0.1 M KOH; these values are higher than those of the state-of-the-art precious-metal IrO_2 catalyst and other well-known perovskites, such as BSCF and SCO. This low-cost material exhibits an open porous topographical structure and as a result, has a large specific surface area of 26 $m^2\cdot g^{-1}$, which is 5 times larger than that of the sample obtained using a solid-state method. Specially, it could be confirmed that the interior surface of a porous structure has much higher OER activity than the external surface of a particle. We also found that the molten-salt approach yields a higher eco-efficiency than the conventional solid-state approach by lowering the calcination temperature from 1,200 to 850 °C as well as by shortening the sintering time from 10 to 5 h. It was found that both the iron content and molten-salt approach play important roles in producing porous structures in LSCF perovskite oxides. These results not only illustrate the potential of porous LSCF28 as an efficient and low-cost OER electrocatalyst, but also demonstrate that the molten-salt approach is a new and efficient approach to develop and mass-produce highly active perovskite oxides.

Acknowledgements

We thank Hong-Ji Lin and Chien-Te Chen's help for the soft X-ray absorption spectroscopy experiments in National Synchrotron Radiation Research Center (NSRRC). This work was partly supported by the National Natural Science Foundation of China (Nos. 11305250 and 11575280), the Joint Funds of the National Natural Science Foundation of China (No. U1232117), the Key Project of Science and Technology of Shanghai (No. 15DZ1200100), and the Youth Innovation Promotion Association of the Chinese Academy of Sciences (Nos. 2014237 and 2015212).

Electronic Supplementary Material: Supplementary material (further details of the electrochemical calculation, AXS fitting details, electrochemical measurements, and SEM imaging additional materials characterization) is available in the online version of this article at https://doi.org/10.1007/s12274-018-2065-1.

References

[1] Chu, S.; Majumdar, A. Opportunities and challenges for a sustainable energy future. *Nature* **2012**, *488*, 294–303.

[2] Cook, T. R.; Dogutan, D. K.; Reece, S. Y.; Surendranath, Y.; Teets, T. S.; Nocera, D. G. Solar energy supply and storage for the legacy and nonlegacy worlds. *Chem. Rev.* **2010**, *110*, 6474–6502.

[3] Montoya, J. H.; Seitz, L. C.; Chakthranont, P.; Vojvodic, A.; Jaramillo, T. F.; Nørskov, J. K. Materials for solar fuels and chemicals. *Nat. Mater.* **2017**, *16*, 70–81.

[4] Koper, M. T. M. Hydrogen electrocatalysis: A basic solution. *Nat. Chem.* **2013**, *5*, 255–256.

[5] Gasteiger, H. A.; Marković, N. M. Just a dream—or future reality? *Science.* **2009**, *324*, 48–49.

[6] Gorlin, Y.; Jaramillo, T. F. A bifunctional nonprecious metal catalyst for oxygen reduction and water oxidation. *J. Am. Chem. Soc.* **2010**, *132*, 13612–13614.

[7] Seh, Z. W.; Kibsgaard, J.; Dickens, C. F.; Chorkendorff, I.; Nørskov, J. K.; Jaramillo, T. F. Combining theory and experiment in electrocatalysis: Insights into materials design. *Science* **2017**, *355*, eaad4998.

[8] Gong, M.; Wang, D.-Y.; Chen, C.-C.; Hwang, B.-J.; Dai, H. J. A mini review on nickel-based electrocatalysts for alkaline hydrogen evolution reaction. *Nano Res.* **2016**, *9*, 28–46.

[9] Chen, D. J.; Chen, C.; Baiyee, Z. M.; Shao, Z. P.; Ciucci, F. Nonstoichiometric oxides as low-cost and highly-efficient oxygen reduction/evolution catalysts for low-temperature electrochemical devices. *Chem. Rev.* **2015**, *115*, 9869–9921.

[10] Bao, J.; Zhang, X. D.; Fan, B.; Zhang, J. J.; Zhou, M.; Yang, W. L.; Hu, X.; Wang, H.; Pan, B. C.; Xie, Y. Ultrathin spinel-structured nanosheets rich in oxygen deficiencies for enhanced electrocatalytic water oxidation. *Angew.Chem.* **2015**, *127*, 7507–7512.

[11] Nai, J. W.; Yin, H. J.; You, T. T.; Zheng, L. R.; Zhang, J.; Wang, P. X.; Jin, Z.; Tian, Y.; Liu, J. Z.; Tang, Z. Y. et al. Efficient electrocatalytic water oxidation by using amorphous Ni-Co double hydroxides nanocages. *Adv. Energy Mater.* **2015**, *5*, 1401880.

[12] Correa-Baena, J. P.; Saliba, M.; Buonassisi, T.; Grätzel, M.; Abate, A.; Tress, W.; Hagfeldt, A. Promises and challenges of perovskite solar cells. *Science* **2017**, *358*, 739–744.

[13] Fabbri, E.; Nachtegaal, M.; Binninger, T.; Cheng, X.; Kim, B. J.; Durst, J.; Bozza, F.; Graule, T.; Schäublin, R.; Wiles, L. et al. Dynamic surface self-reconstruction is the key of highly active perovskite nano-electrocatalysts for water splitting. *Nat. Mater.* **2017**, *16*, 925–931.

[14] Royer, S.; Duprez, D.; Can, F.; Courtois, X.; Batiot-Dupeyrat, C.; Laassiri, S.; Alamdari, H. Perovskites as substitutes of noble metals for heterogeneous catalysis: Dream or reality. *Chem. Rev.* **2014**, *114*, 10292–10368.

[15] Zhu, Y. L.; Zhou, W.; Yu, J.; Chen, Y. B.; Liu, M. L.; Shao, Z. P. Enhancing electrocatalytic activity of perovskite oxides by tuning cation deficiency for oxygen reduction and evolution reactions. *Chem. Mater.* **2016**, *28*, 1691–1697.

[16] Yan, Z. H.; Sun, H. M.; Chen, X.; Fu, X. R.; Chen, C. C.; Cheng, F. Y.; Chen, J. Rapid low-temperature synthesis of perovskite/carbon nanocomposites as superior electrocatalysts for oxygen reduction in Zn-air batteries. *Nano Res.*, in press, DOI: 10.1007/s12274-017-1869-8.

[17] Zhu, Y. L.; Zhou, W.; Shao, Z. P. Perovskite/carbon composites: Applications in oxygen electrocatalysis. *Small.* **2017**, *13*, 1603793.

[18] Suntivich, J.; May, K. J.; Gasteiger, H. A.; Goodenough, J. B.; Shao-Horn, Y. A perovskite oxide optimized for oxygen evolution catalysis from molecular orbital principles. *Science* **2011**, *334*, 1383–1385.

[19] Suntivich, J.; Gasteiger, H. A.; Yabuuchi, N.; Nakanishi, H.; Goodenough, J. B.; Shao-Horn, Y. Design principles for oxygen-reduction activity on perovskite oxide catalysts for fuel cells and metal–air batteries. *Nat. Chem.* **2011**, *3*, 546–550.

[20] Zhu, Y. L.; Zhou, W.; Zhong, Y. J.; Bu, Y. F.; Chen, X. Y.; Zhong, Q.; Liu, M. L.; Shao, Z. P. A perovskite nanorod as bifunctional electrocatalyst for overall water splitting. *Adv. Energy Mater.* **2017**, *7*, 1602122.

[21] Mefford, J. T.; Rong, X.; Abakumov, A. M.; Hardin, W. G.; Dai, S.; Kolpak, A. M.; Johnston, K. P.; Stevenson, K. J. Water electrolysis on $La_{1-x}Sr_xCoO_{3-\delta}$ perovskite electrocatalysts. *Nat. Commun.* **2016**, *7*, 11053.

[22] Zhou, S. M.; Miao, X. B.; Zhao, X.; Ma, C.; Qiu, Y. H.; Hu, Z. P.; Zhao, J. Y.; Shi, L.; Zeng, J. Engineering electrocatalytic activity in nanosized perovskite cobaltite through surface spin-state transition. *Nat. Commun.* **2016**, *7*, 11510.

[23] Chen, G.; Zhou, W.; Guan, D. Q.; Sunarso, J.; Zhu, Y. P.; Hu, X. F.; Zhang, W.; Shao, Z. P. Two orders of magnitude enhancement in oxygen evolution reactivity on amorphous $Ba_{0.5}Sr_{0.5}Co_{0.8}Fe_{0.2}O_{3-\delta}$ nanofilms with tunable oxidation state. *Sci. Adv.* **2017**, *3*, e1603206.

[24] Zhu, Y. L.; Zhou, W.; Sunarso, J.; Zhong, Y. J.; Shao, Z. P. Phosphorus-doped perovskite oxide as highly efficient water oxidation electrocatalyst in alkaline solution. *Adv. Funct. Mater.* **2016**, *26*, 5862–5872.

[25] Grimaud, A.; May, K. J.; Carlton, C. E.; Lee, Y.-L.; Risch, M.; Hong, W. T.; Zhou, J.; Shao-Horn, Y. Double perovskites as a family of highly active catalysts for oxygen evolution in alkaline solution. *Nat. Commun.* **2013**, *4*, *2439*.

[26] Yagi, S.; Yamada, I.; Tsukasaki, H.; Seno, A.; Murakami, M.; Fujii, H.; Chen, H.; Umezawa, N.; Abe, H.; Nishiyama, N.; Mori, S. Covalency-reinforced oxygen evolution reaction catalyst. *Nat. Commun.* **2015**, *6*, 8249.

[27] Shao, Z. P.; Zhou, W.; Zhu, Z. H. Advanced synthesis of materials for intermediate-temperature solid oxide fuel cells. *Progress in Mater. Sci.* **2012**, *57*, 804–874.

[28] Zhu, Y. L.; Zhou, W.; Chen, Z.-G.; Chen, Y. B.; Su, C.; Tadé, M. O.; Shao, Z. P. $SrNb_{0.1}Co_{0.7}Fe_{0.2}O_{3-\delta}$ perovskite as a next-generation electrocatalyst for oxygen evolution in alkaline solution. *Angew. Chem., Int. Ed.* **2015**, *54*, 3897–3901.

[29] Lee, J. J.; Oh, M. Y.; Nahm, K. S. Effect of ball milling on electrocatalytic activity of perovskite $La_{0.6}Sr_{0.4}CoO_{3-\delta}$ applied for lithium air battery. *J. Electrochem. Soc.* **2016**, *163*, A244–A250.

[30] Hashimoto, S.-I.; Fukuda, Y.; Kuhn, M.; Sato, K.; Yashiro, K.; Mizusaki, J. Thermal and chemical lattice expansibility of $La_{0.6}Sr_{0.4}Co_{1-y}Fe_yO_{3-\delta}$ (y = 0.2, 0.4, 0.6 and 0.8). *Solid State Ionics* **2011**, *186*, 37–43.

[31] Heel, A.; Holtappels, P.; Hug, P.; Graule, T. Flame spray synthesis of nanoscale $La_{0.6}Sr_{0.4}Co_{0.2}Fe_{0.8}O_{3-\delta}$ and $Ba_{0.5}Sr_{0.5}Co_{0.8}Fe_{0.2}O_{3-\delta}$ as cathode materials for intermediate temperature solid oxide fuel cells. *Fuel Cells.* **2010**, *10*, 419–432.

[32] Dieterle, L.; Bockstaller, P.; Gerthsen, D.; Hayd, J.; Ivers-Tiffée, E.; Guntow, U. Microstructure of nanoscaled $La_{0.6}Sr_{0.4}CoO_{3-\delta}$ cathodes for intermediate-temperature solid oxide fuel cells. *Adv. Energy Mater.* **2011**, *1*, 249–258.

[33] Morán-Ruiz, A.; Vidal, K.; Larrañaga, A.; Arriortua, M. I. Chemical compatibility and electrical contact of $LaNi_{0.6}Co_{0.4}O_{3-\delta}$ (LNC) between Crofer22APU interconnect and $La_{0.6}Sr_{0.4}FeO_3$ (LSF) cathode for IT-SOFC. *Fuel Cells* **2013**, *13*, 398–403.

[34] Natile, M. M.; Poletto, F.; Galenda, A.; Glisenti, A.; Montini, T.; De Rogatis, L.; Fornasiero, P. $La_{0.6}Sr_{0.4}Co_{1-y}Fe_yO_{3-\delta}$ perovskites: Influence of the Co/Fe atomic ratio on properties and catalytic activity toward alcohol steam-reforming. *Chem. Mater.* **2008**, *20*, 2314–2327.

[35] Shannon, R. D. Revised effective ionic radii and systematic studies of interatomic distances in halides and chalcogenides. *Acta Crystallogr. Section A* **1976**, *32*, 751–767.

[36] Wang, Y. C.; Zhou, T.; Jiang, K.; Da, P. M.; Peng, Z.; Tang, J.; Kong, B.; Cai, W.-B.; Yang, Z. Q.; Zheng, G. F. Reduced mesoporous Co_3O_4 nanowires as efficient water oxidation electrocatalysts and supercapacitor electrodes. *Adv. Energy Mater.* **2014**, *4*, 1400696.

[37] Kruk, M.; Jaroniec, M.; Ko, C. H.; Ryoo, R. Characterization of the porous structure of SBA-15. *Chem. Mater.* **2000**, *12*, 1961–1968.

[38] Liu, X. F.; Antonietti, M. Moderating black powder chemistry for the synthesis of doped and highly porous graphene nanoplatelets and their use in electrocatalysis. *Adv. Mater.* **2013**, *25*, 6284–6290.

[39] Mao, Y. B.; Banerjee, S.; Wong, S. S. Large-scale synthesis of single-crystalline perovskite nanostructures. *J. Am. Chem. Soc.* **2003**, *125*, 15718–15719.

[40] Kang, J. S.; Lee, H. J.; Kim, G.; Kim, D. H.; Dabrowski, B.; Kolesnik, S.; Lee, H.; Kim, J. Y.; Min, B. I. Electronic structure of the cubic perovskite $SrMn_{1-x}Fe_xO_3$ investigated by X-ray spectroscopies. *Phys. Rev. B* **2008**, *78*, 154434.

[41] Lin, H. J.; Chin, Y. Y.; Hu, Z.; Shu, G. J.; Chou, F. C.; Ohta, H.; Yoshimura, K.; Hebert, S.; Maignan, A.; Tanaka, A. et al. Local orbital occupation and energy levels of Co in Na_xCoO_2: A soft X-ray absorption study. *Phy. Rev. B* **2010**, *81*, 115138.

[42] Zhang, B.; Zheng, X. L.; Voznyy, O.; Comin, R.; Bajdich, M.; Garcia-Melchor, M.; Han, L. L.; Xu, J. X.; Liu, M.; Zheng, L. R. et al. Homogeneously dispersed multimetal oxygen-evolving catalysts. *Science* **2016**, *352*, 333–337.

[43] Hong, W. T.; Stoerzinger, K. A.; Lee, Y.-L.; Giordano, L.; Grimaud, A.; Johnson, A. M.; Hwang, J.; Crumlin, E. J.; Yang, W.; Shao-Horn, Y. Charge-transfer-energy-dependent oxygen evolution reaction mechanisms for perovskite oxides. *Energy Environ. Sci.* **2017**, *10*, 2190–2200.

[44] Luo, K.; Roberts, M. R.; Hao, R.; Guerrini, N.; Pickup, D. M.; Liu, Y. S.; Edström, K.; Guo, J.; Chadwick, A. V.; Duda, L. C. et al. Charge-compensation in 3D-transition-metal-oxide intercalation cathodes through the generation of localized electron holes on oxygen. *Nat. Chem.* **2016**, *8*, 684–691.

[45] Zhang, H.; Liu, J. Y.; Zhao, G. Q.; Gao, Y. J.; Tyliszczak, T.; Glans, P. A.; Guo, J. H.; Ma, D.; Sun, X. H.; Zhong, J. Probing the interfacial interaction in layered-carbon-stabilized iron oxide nanostructures: A soft X-ray spectroscopic study. *ACS Appl. Mater. Interfaces* **2015**, *7*, 7863–7868.

[46] Zheng, X. L.; Zhang, B.; De Luna, P.; Liang, Y. F.; Comin, R.; Voznyy, O.; Han, L. L.; de Arquer, F. P. G.; Liu, M.; Dinh, C. T. et al. Theory-driven design of high-valence metal sites for water oxidation confirmed using *in situ* soft X-ray absorption. *Nat. Chem.* **2018**, *10*, 149–154.

[47] Wilson, S. A.; Kroll, T.; Decreau, R. A.; Hocking, R. K.; Lundberg, M.; Hedman, B.; Hodgson, K. O.; Solomon, E. I. Iron L-edge X-ray absorption spectroscopy of oxy-picket fence porphyrin: Experimental insight into Fe–O_2 bonding. *J. Am. Chem. Soc.* **2013**, *135*, 1124–1136.

[48] Mizokawa, T.; Wakisaka, Y.; Sudayama, T.; Iwai, C.; Miyoshi, K.; Takeuchi, J.; Wadati, H.; Hawthorn, D. G.; Regier, T. Z.; Sawatzky, G. A. Role of oxygen holes in $LixCoO_2$ revealed by soft X-ray spectroscopy. *Phy. Rev. Let.* **2013**, *111*, 056404.

[49] Chen, J.-M.; Chin, Y.-Y.; Valldor, M.; Hu, Z. W.; Lee, J.-M.; Haw, S.-C.; Hiraoka, N.; Ishii, H.; Pao, C.-W.; Tsuei, K.-D. et al. A complete high-to-low spin state transition of trivalent cobalt ion in octahedral symmetry in $SrCo_{0.5}Ru_{0.5}O_{3-\delta}$. *J. Am. Chem. Soc.* **2014**, *136*, 1514–1519.

[50] Xu, L.; Jiang, Q. Q.; Xiao, Z. H.; Li, X. Y.; Huo, J.; Wang, S. Y.; Dai, L. M. Plasma-engraved Co_3O_4 nanosheets with oxygen vacancies and high surface area for the oxygen evolution reaction. *Angew. Chem.* **2016**, *128*, 5363–5367.